Science Advances

AAAS

Supplementary Materials for

Paleomagnetic evidence for a disk substructure in the early solar system

Cauê S. Borlina*, Benjamin P. Weiss, James F. J. Bryson, Xue-Ning Bai,
Eduardo A. Lima, Nilanjan Chatterjee, Elias N. Mansbach

*Corresponding author. Email: caue@mit.edu

This PDF file includes:

Supplementary Text
Figs. S1 to S11
Tables S1 to S6
References

Supplementary Text

1. Formation Region of Chondrules from the Carbonaceous Chondrites

The existence of a dichotomy in various isotopic systems (e.g., Ti, Mo, Cr, O, Ru, W, Ni) for bulk meteorite samples provides evidence that carbonaceous and non-carbonaceous meteorites may have formed in two distinct reservoirs (*2*, *3*). An equivalent dichotomy is also observed between chondrules from ordinary chondrites [i.e., LL chondrules (*11*)] and carbonaceous chondrites [i.e., CO chondrules (*3*, *55*, *56*)]. The exact location and nature of these reservoirs is still under debate. Nonetheless, because carbonaceous chondrites are likely derived from the water rich C-type asteroids (*57*, *58*), we take their current location at >3 AU as a reference for the location of the carbonaceous reservoir in the early solar system. Furthermore, measurements of the isotopic composition of water in carbonaceous meteorites suggests that most of these samples did not originate beyond 7 AU (*59*). Finally, astronomical observations indicate that meteorites and their components likely formed in the midplane region of the protoplanetary disk (*10*, *60*). Thus, we take the formation region of the CO chondrules to be somewhere between 3-7 AU in the midplane of the early solar system. These regions are similar to, although more restrictive than, the formation regions envisaged by ref. (*6*) and less restrictive than estimated by ref. (*61*).

2. Paleomagnetic Tests to Determine the Origin of the Magnetization

Two paleomagnetic tests were conducted to determine the robustness and the origin of the high coercivity (HC) magnetization of the chondrules: the unidirectionality test and the conglomerate test (*11*). For a magnetization acquired by a chondrule in a uniform background field, we expect subsamples of the same chondrule to have HC paleodirections within error of one another. To test this, we split three chondrules (DOC3, DOC5, and DOC6) into two mutually oriented pieces, each of which we then AF demagnetized and measured (Fig. 2). Comparing the HC directions for the subsamples from each chondrule, we found that all three pairs of subsamples have internally consistent HC magnetization orientations, with mean directions within each other's MADs, supporting our conclusion that the dusty olivine chondrules acquired a stable, homogeneous TRM.

The conglomerate test establishes whether chondrules have been remagnetized since their accretion onto the CO parent body. Remagnetization can occur due to post-accretional thermal metamorphism and/or aqueous alteration on the parent body, heating during atmospheric entry, secondary magnetic minerals produced during terrestrial weathering, and/or and isothermal remanent magnetization (IRM) during sample handling. Because the chondrules were accreted onto the parent body in random directions, chondrules that have not been remagnetized since accretion should exhibit random HC directions. This is indeed what we observe (Fig. 2). Using Eqs. (3) and (4) from ref. (*34*), we calculated the critical value R_0 that the resultant of N nonrandomly oriented unit vectors exceeds 95% of the time. We then we compared this with the length of the resultant of the HC vectors for chondrules from each meteorite, R. When $R < R_0$, we cannot reject the hypothesis that the vectors are random with 95% confidence. Table S2 summarizes the results for the chondrules from ALHA 77307 and DOM 08006, showing that the random hypothesis cannot be rejected with 95% confidence for both samples. This shows that chondrules from both samples were not remagnetized since their accretion to the parent body.
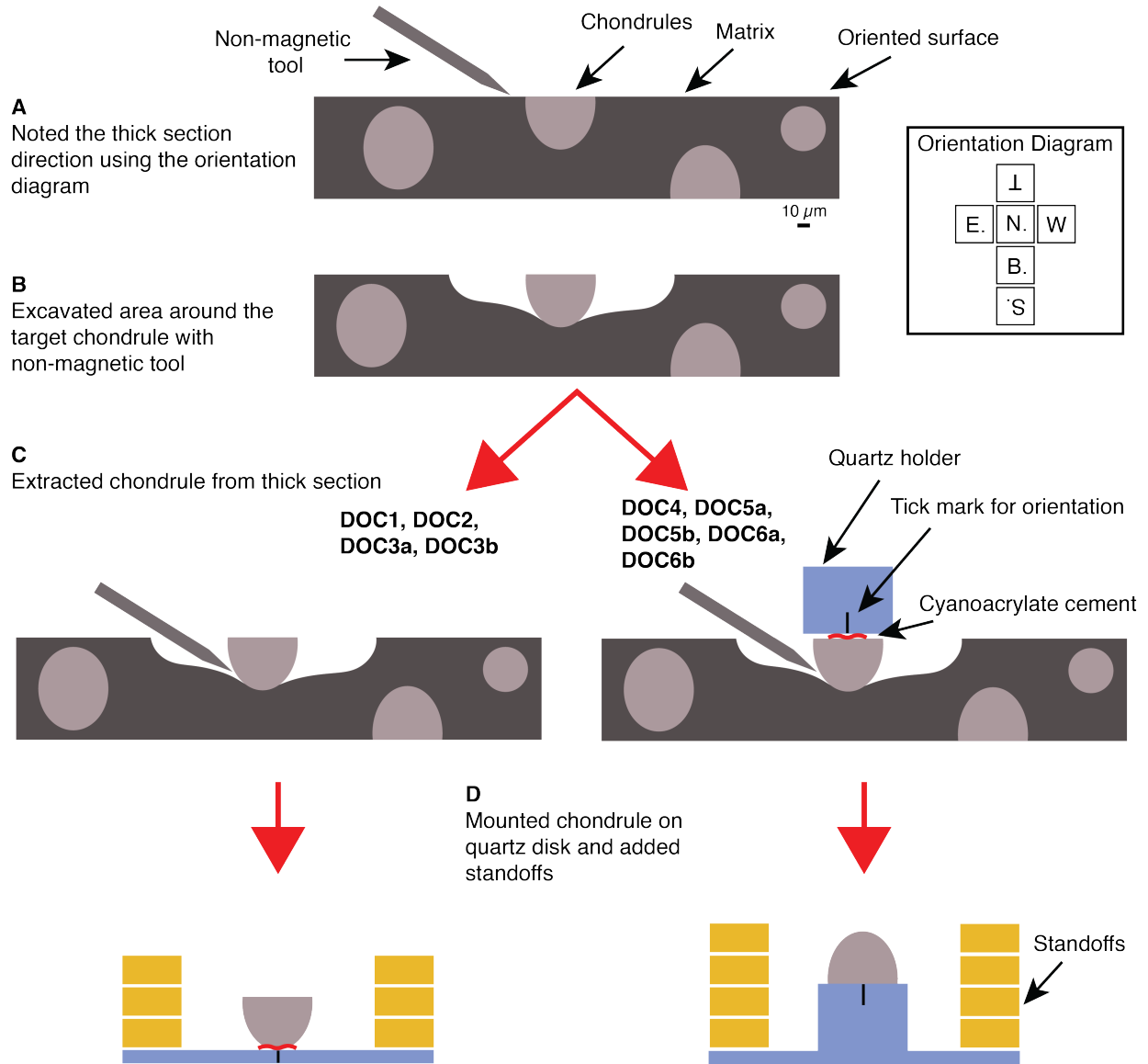
Fig. S1. Schematic showing the sample mounting procedure. (A) Oriented thick sections from the meteorites ALHA 77307 and DOM 08006 were cut and then polished. Dusty olivine targets were identified using reflective light. Orientation diagram is shown on the top right. **(B)** A region around the sample was excavated prior to chondrule extraction. **(C)** Chondrules were extracted using two methods described in the text. **(D)** Samples were mounted on nonmagnetic quartz disks with standoffs to protect sample from rubbing against the SQUID microscope window.

3. Mineralogy of the chondrules

Fig. S4 shows the BSE images (Figs. S4A and D) together with interpretations of the WDS data (Figs. S4B and E) for each sample. Tables S3-S4 summarize the measurements from the WDS analyses for distinct grains. In both samples, we observe the presence of micrometer and sub-micrometer sized Fe kamacite (α-Fe) inclusions in forsterite (Tables S3 and S4) supporting the identification of these inclusions as dusty olivine chondrules (*25*). In DOC2, only we also observed
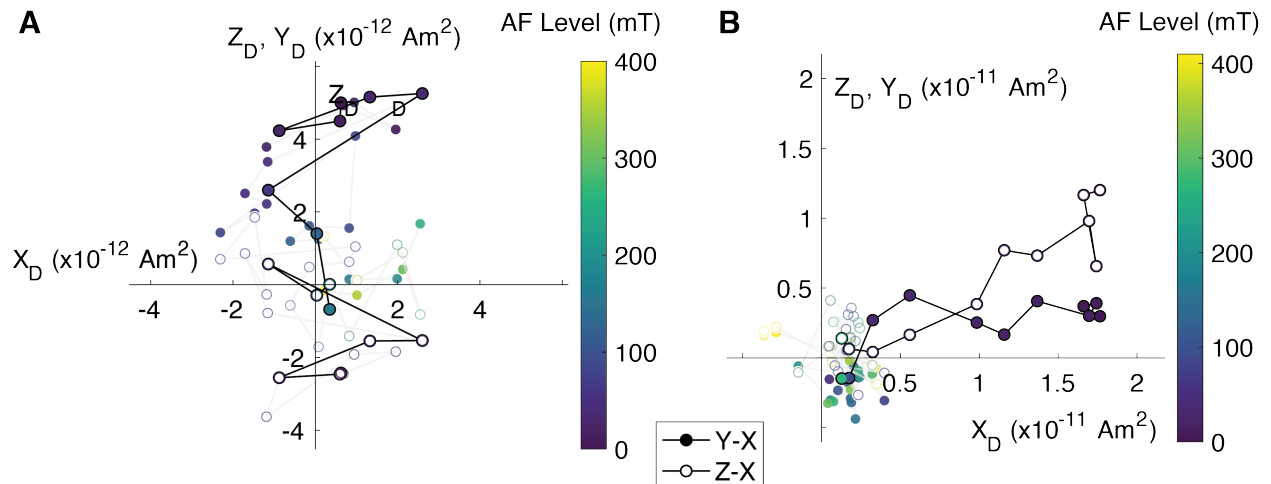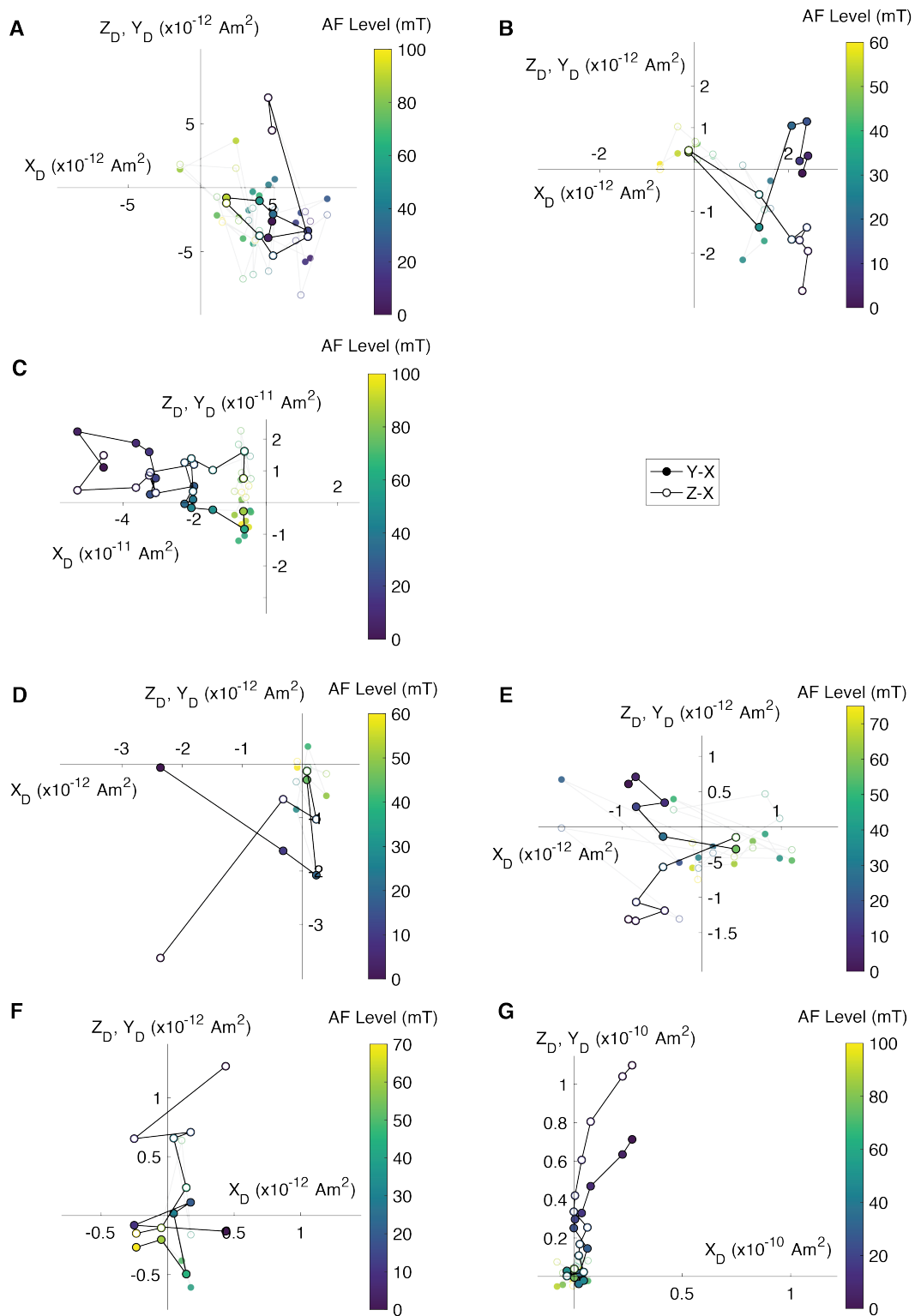
Fig. S2. AF demagnetization of dusty olivine chondrules from ALHA 77307. (A) DOC1. **(B)** DOC2. Shown are orthographic projections of the NRM vector endpoints. Closed symbols show the Y-X projection of the moment; open symbols show Z-X projection of the moment. Samples were oriented in the same coordinate system as samples shown in Fig. 1A-B. Colorbar shows the AF level of the steps. Opaque symbols denote datapoints averaged across multiple AF levels while semi-transparent symbols denote unaveraged data. Averaged levels are summarized in the Table S1.

a single martensite (α_2-Fe$_{68}$Ni$_{20}$) and single magnetite inclusion, with the latter likely associated with minor alteration on the parent-body.

Figs. S4C and S4F show quantum diamond microscopy (QDM) maps showing demagnetized NRM (Fig. S4C) and an ARM acquisition (Fig. S4F) of the same samples that we obtained BSE images and conducted WDS analysis. We observe from both maps that the distribution of the magnetic field is uniform, consistent with the presence of fine Fe grains distributed uniformly throughout the sample's volumes. This spatial distribution is characteristic of the iron metal in dusty olivine chondrules. These maps are also inconsistent with large concentrations of Fe on the grain exterior and/or along cracks where secondary minerals typically form during aqueous alteration. Overall, these observations further support our conclusion that these chondrules contain a magnetic record of the nebular field formed prior to their accretion on the parent body.

4. Assessing Remanence Anisotropy

Anisotropy in samples can bias paleointensity and paleodirection estimates (*62*). To establish if our chondrules required anisotropy corrections, we conducted consecutive ARM acquisitions for each chondrule. Fig. S7 shows ARM acquisitions in a 200 µT bias field for the samples from which we obtained paleointensities. We used an AC field of 400 mT for DOC1, 410 mT for DOC2, 100 mT for DOC3a, 60 mT for DOC3b, 100 mT for DOC4, 60 mT for DOC5a, 75 mT for DOC 5b, 70 mT for DOC 6a, and 100 mT for DOC6b. For samples DOC1, DOC2, DOC3a, DOC3b and DOC4, the applied direction of the ARM was directly in the -*z* direction. For samples DOC5b and DOC6b the direction of the applied ARM was in the +*z* direction. Overall, the direction of the acquired ARM is within 15% of the direction of applied field for all samples. Because of this, we chose not to apply an anisotropy correction to any of our samples.

Fig. S3. AF demagnetization of dusty olivine chondrules from DOM 08006. (**A**) DOC3a. (**B**) DOC3b. (**C**) DOC4. (**D**) DOC5a. (**E**) DOC5b (**F**) DOC6a. (**G**) DOC6b. Shown are orthographic projections of the NRM vector endpoints. Closed symbols show the Y-X projection of the moment; open symbols show Z-X projection of the moment. Samples were oriented in the same coordinate system as the samples in Fig. 1C-D. Colorbar shows the AF levels of the steps. Opaque symbols denote datapoints averaged across multiple AF levels while semi-transparent symbols denote unaveraged data. Averaged levels are summarized in the Table S1.
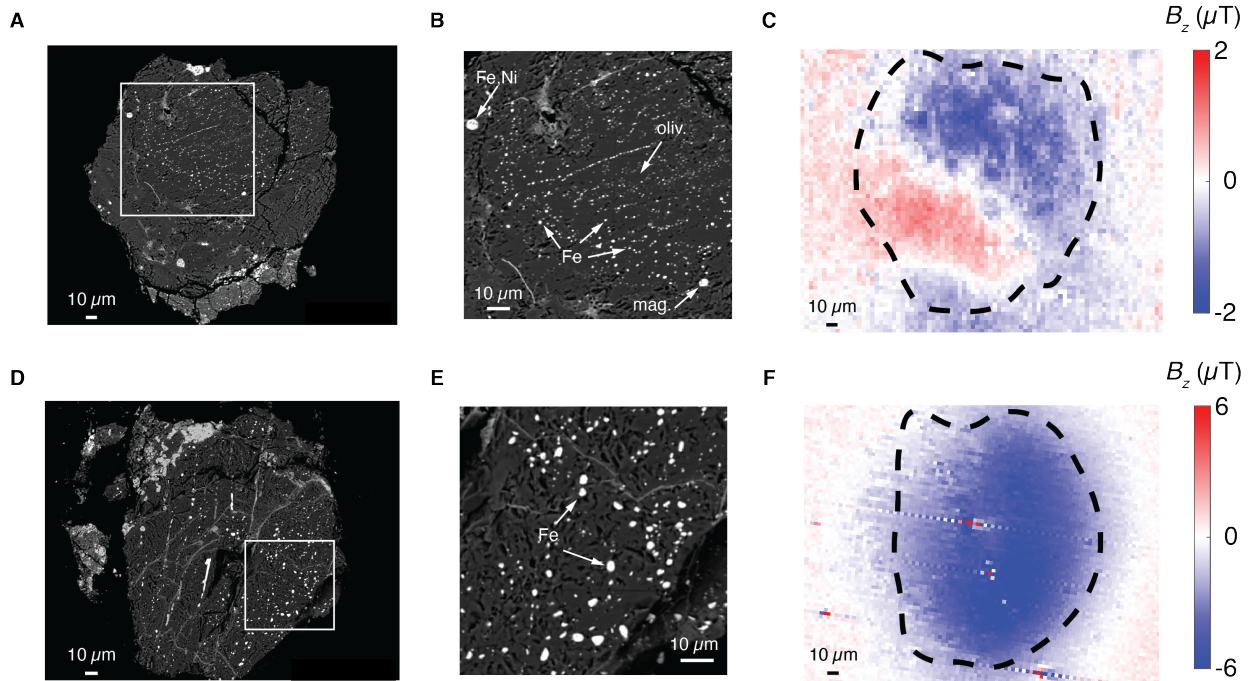
Fig. S4. BSE images, WDS analysis and QDM maps for samples DOC2 (A-C) and DOC6b (D-F). (A and D) BSE images with a white square showing the zoom in for (B) and (E). **(B and E)** Magnified view of the BSE images in (A) and (D). WDS analysis shows the presence of pure Fe in forsterite (oliv.) indicating that these samples are dusty olivine grains. We also observe the presence of Fe,Ni metal inclusions and a magnetite (mag.) inclusion in the sample. **(C and F)** QDM maps of the samples with dashed lines depicting the outline of the grains shown in (A) and (D). (C) QDM map showing the last step of the demagnetization of a 200 µT ARM. (F) QDM maps showing an ARM application (DC field 200 µT, AC field 100 mT) oriented in the into-the-page direction. The saturation points in the QDM map are artifacts from the diamond. In both maps, the magnetization originates from the region where the dusty olivine Fe grains are located.

5. Temporal or spatial variation?

To determine the probability that the measurements from the non-carbonaceous reservoir (*11*) and those obtained in this study from the carbonaceous reservoir reflect a temporal variation in the accretion rate, we conducted two numerical experiments using Monte Carlo simulations. Specifically, we sought to test the hypothesis that a single step change in the magnetic field and, by implication in the accretion rate, at some time t^* could explain the differences in accretion rates inferred from LL versus CO chondrules. A step change in the field is a limiting case because, if optimally timed, it would be more likely to produce a larger difference in average paleointensity between the two groups of chondrules than higher frequency field variations.

We started by fitting a normal distribution to the Al-Mg ages of the chondrules from Semarkona (LL3.0) and Y-81020 (CO3.0) (*12*). For Semarkona, we obtained a mean $\mu = 2.0$ Ma after CAI-formation and standard deviation $\sigma = 0.4$ Ma, while for Y-81020 we obtained a mean $\mu = 2.2$ Ma after CAI-formation and standard deviation $\sigma = 0.4$ Ma. For the first experiment, we randomly drew 5 ages [the number of chondrules used in ref. (*11*) to determine the mean LL dusty olivine chondrule paleointensity] from the normal distribution of LL ages to represent the LL chondrules from the non-carbonaceous reservoir. Similarly, we randomly drew 7 ages (the number
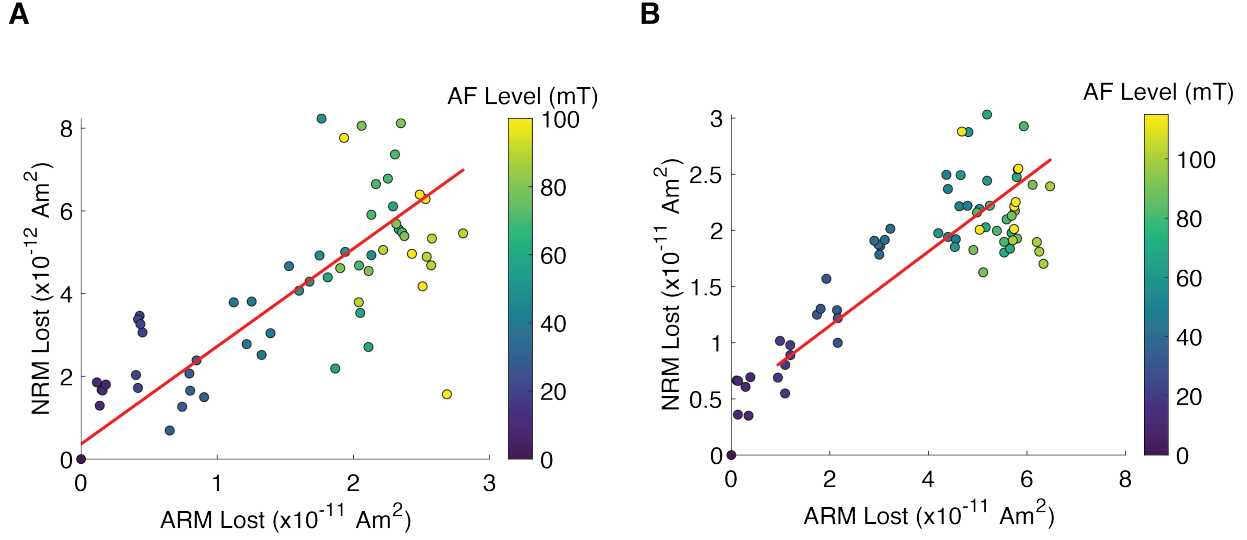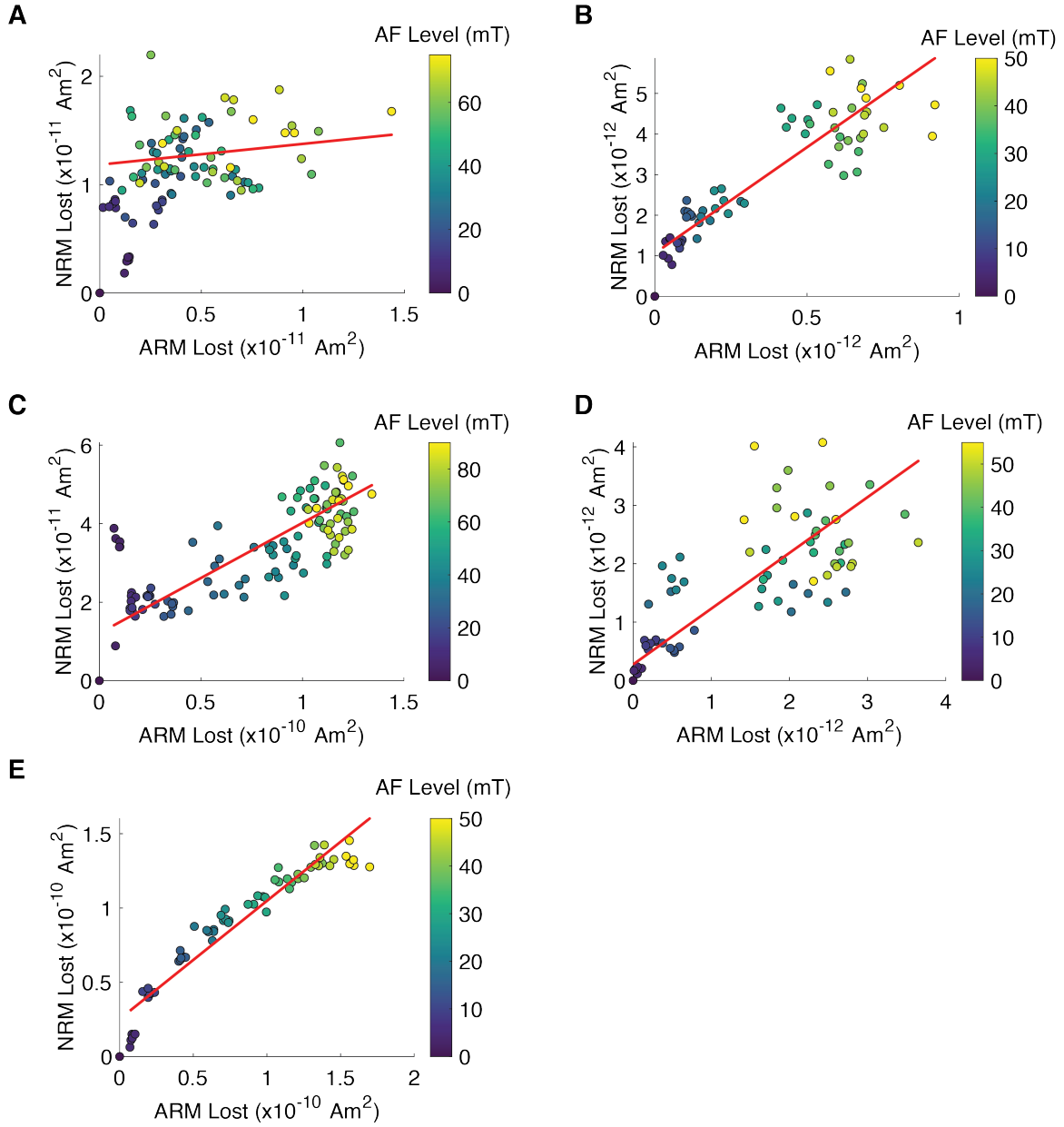
Fig. S5. Paleointensity experiments for ALHA 77307. Shown is NRM lost versus ARM lost during AF demagnetization of dusty olivine chondrules. (**A**) DOC1. (**B**) DOC2. Red line shows the least squares fit over the coercivity range used to calculate the paleointensity. Table S5 shows the paleointensity and the 95% confidence interval for the fit.

of chondrules used to determine the paleointensity in this study) from the normal distribution of CO ages to represent the chondrules we measured from the carbonaceous reservoir. The random sampling from the normal distribution used the function `normrnd` in MATLAB. We repeated this experiment for values of t^* between 1 and 3 Ma after CAI formation to span the range of chondrules ages. Because the LL and CO paleointensities support an aligned configuration between the rotation axis of the disk and the net vertical magnetic field (see main text), we used Eq. (3) from ref. (*10*) taking $f' = 10$ and $m = 10$ to calculate the accretion rates. Using the mean LL paleointensity of 54 µT and a formation region of 2 AU (3), and the mean CO paleointensity of 101 µT from this study with a formation region of 5 AU, we obtained accretion rates of 3.9×10^{-9} solar masses ($M_\odot$) year^{-1} and 1.3×10^{-7} $M_\odot$ year^{-1}, respectively. We took the calculated LL accretion rate as the low accretion rate value ($\dot{M}_\text{low}$), while the calculated CO accretion rate was taken as the high accretion rate value ($\dot{M}_\text{high}$). We identified two scenarios for the step change of the accretion rate: (1) the accretion rate increased at t^* and (2) the accretion rate decreased at t^*. If the randomly selected age was $< t^*$ for the increase/decrease case the low/high accretion rate was assigned. If the randomly selected age $> t^*$, for the increase/decrease case a high/low accretion rate was assigned. We then averaged the accretion rate values for each reservoir and for each case. This experiment was conducted 100,000 times. For each scenario, we calculated the ratio of the mean accretion rate in the carbonaceous reservoir and the mean accretion rate in the non-carbonaceous reservoir. Experiments that had this ratio $\geq \dot{M}_\text{high}/\dot{M}_\text{low} = 1.3 \times 10^{-7}$ $M_\odot$ year^{-1}/3.9×10^{-9} $M_\odot$ year^{-1} ~33 were taken as realizations supporting a time-varying accretion rate in the first 3 Ma after CAI formation. We found that the highest probability of such scenario is 0.37% (Table S6; Figs. S8 and S10A-B).

   We also took a more conservative approach in which we used the $+1\sigma$ upper bound on the LL paleointensities (*11*) of 54 + 21/2 = 64.5 µT to calculate $\dot{M}_\text{low}$ and the mean -1σ lower bound on the CO paleointensities (this study) of 101 – 48/2 = 77 µT to calculate $\dot{M}_\text{high}$. For this case, we

Fig. S6. Paleointensity experiments for DOM 08006. Shown are NRM lost versus ARM lost during AF demagnetization of dusty olivine chondrules. (**A**) DOC3a. (**B**) DOC3b. (**C**) DOC4. (**D**) DOC5b. (**E**) DOC6b. Red line shows the least squares fit over the coercivity range used to calculate the paleointensity. Table S5 shows the paleointensity and the 95% confidence interval for the fit.

also assumed that both samples formed at 3 AU. Using the same equations as before, we obtained $\dot{M}_{\text{low}} = 1.5 \times 10^{-8} \, M_\odot$ year^{-1} and $\dot{M}_{\text{high}} = 2.2 \times 10^{-8}$ s $M_\odot$ year^{-1}. Similarly to the previous analysis, experiments that had the ratio between the mean accretion rate in the carbonaceous reservoir to the mean accretion rate in the non-carbonaceous reservoir $\geq \dot{M}_{\text{high}}/\dot{M}_{low} = 2.2 \times 10^{-8} \, M_\odot$ year^{-1}/$1.5 \times 10^{-8} \, M_\odot$ year^{-1} ~1.46, were taken as realizations that would satisfy that the measured magnetic fields
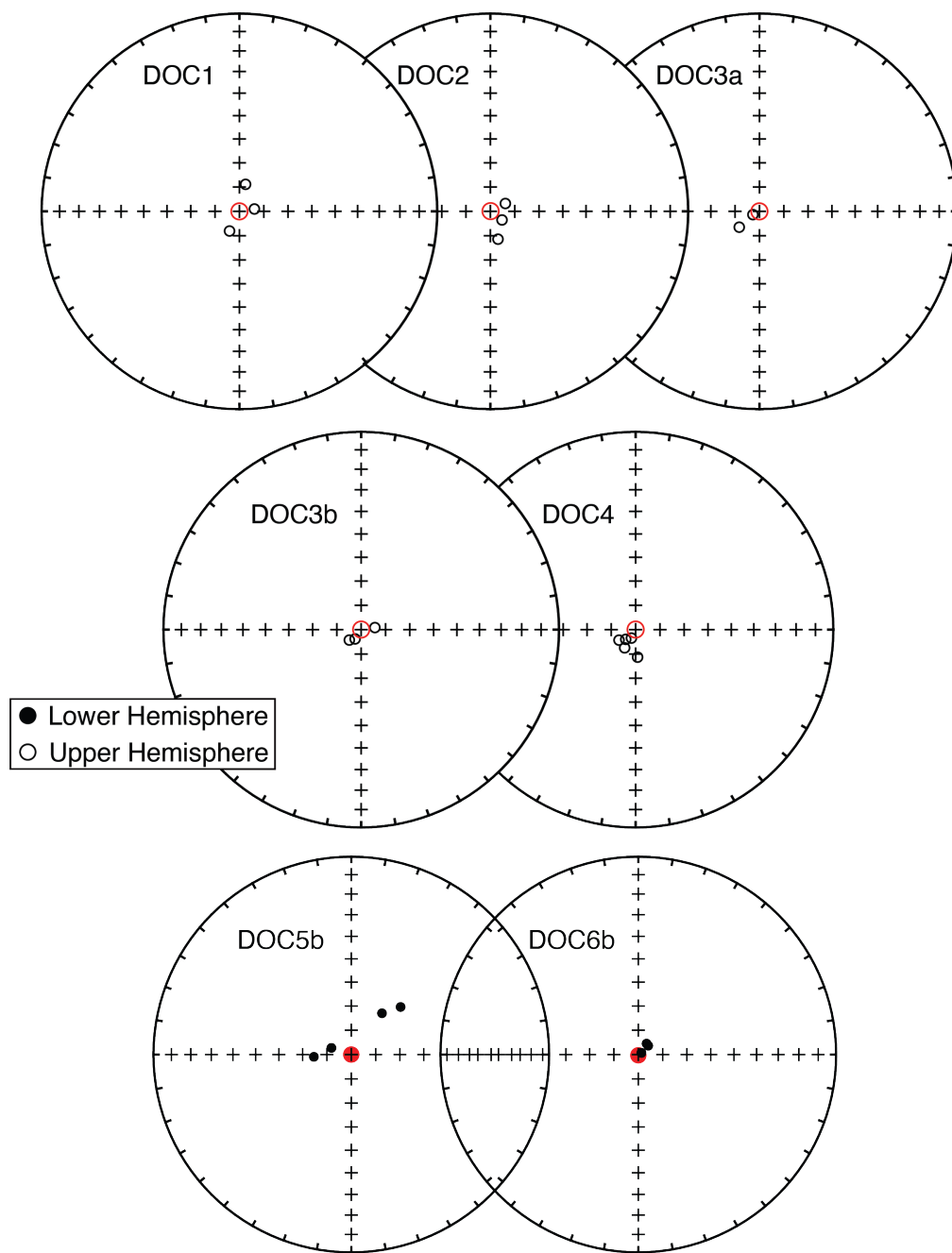
Fig. S7. ARM acquisition by dusty olivine chondrules from ALHA 77307 and DOM 08006. Each datapoint shows the ARM direction with a bias field of 200 µT and AF indicated in section 6. Red circles show the direction of the applied bias magnetic field. We also subtracted the last NRM datapoint from the ARM acquisition.

[from ref. (*11*) and this study] support a time varying accretion rate in the first 3 Ma after CAI formation. The highest probability of such scenario was 0.40% (Table S6; Figs. S9 and S10C-D).

Finally, we also conducted Monte Carlo simulations using recently reported Al-Mg ages with smaller measurement spot sizes for chondrules from Semarkona (*63, 64*) and chondrules from the carbonaceous reservoir (Acfer 094 and Kaba) (*65, 66*). Note that some of these measurements
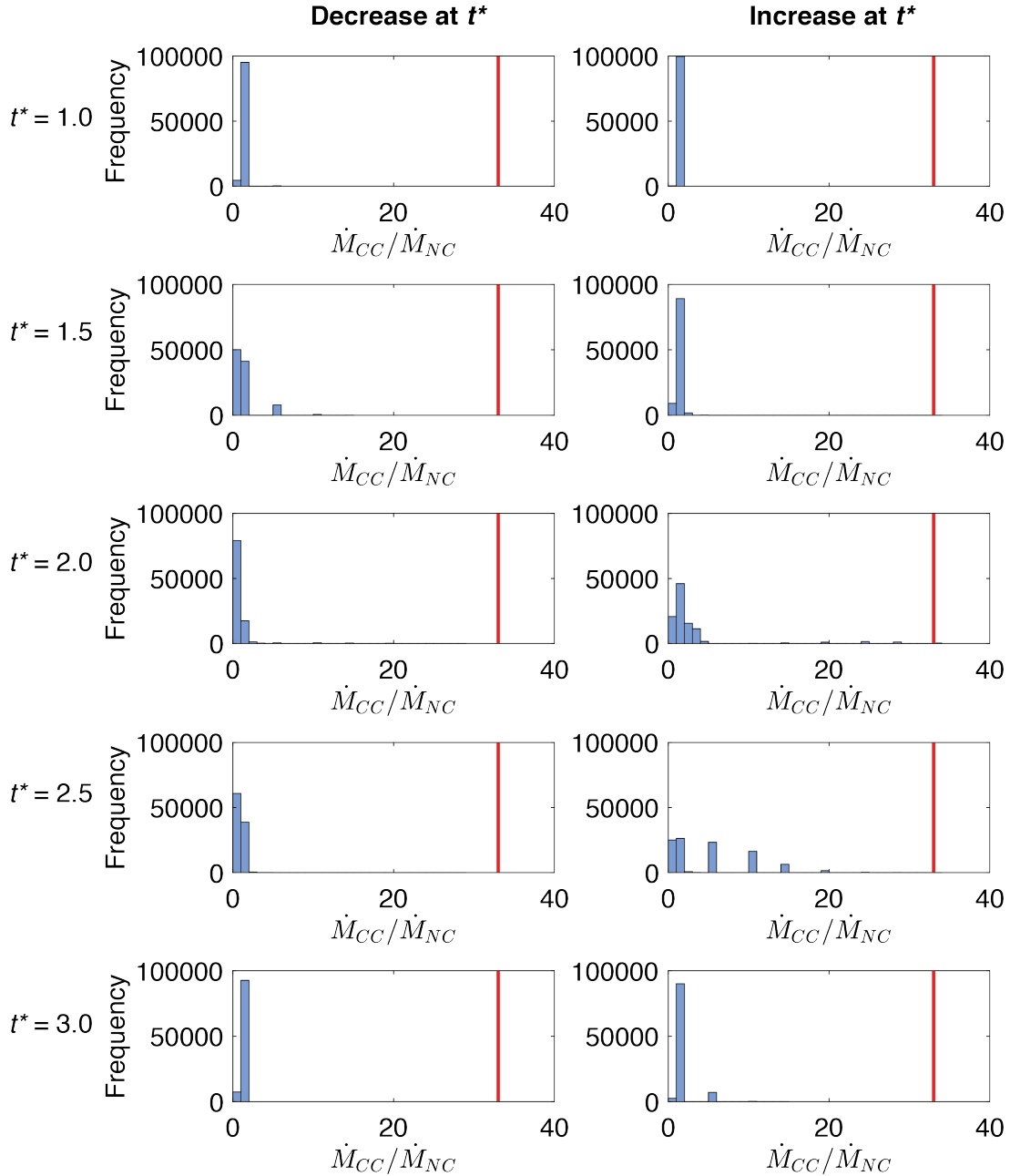
Fig. S8. Monte Carlo simulations assessing the possibility that a temporal change in accretion rates can explain the differences in accretion rates inferred from CO and LL paleointensities. Each plot shows a histogram of the mean accretion rate in the carbonaceous reservoir ($\dot{M}_{CC}$) over the mean accretion rate in the non-carbonaceous reservoir ($\dot{M}_{NC}$). Left column shows simulations for an accretion rate that decreases at t^*. Right column shows simulations for an accretion rate that increases at t^*. From top to bottom are simulations for different choices of t^*. Red line indicates the threshold ratio of 33.

for Y-81020 have only appeared in abstract form. These recent Al-Mg measurements suggest that the formation time of chondrules in the non-carbonaceous and the carbonaceous reservoir were not contemporaneous and that previously reported measurements (*12*) were affected by
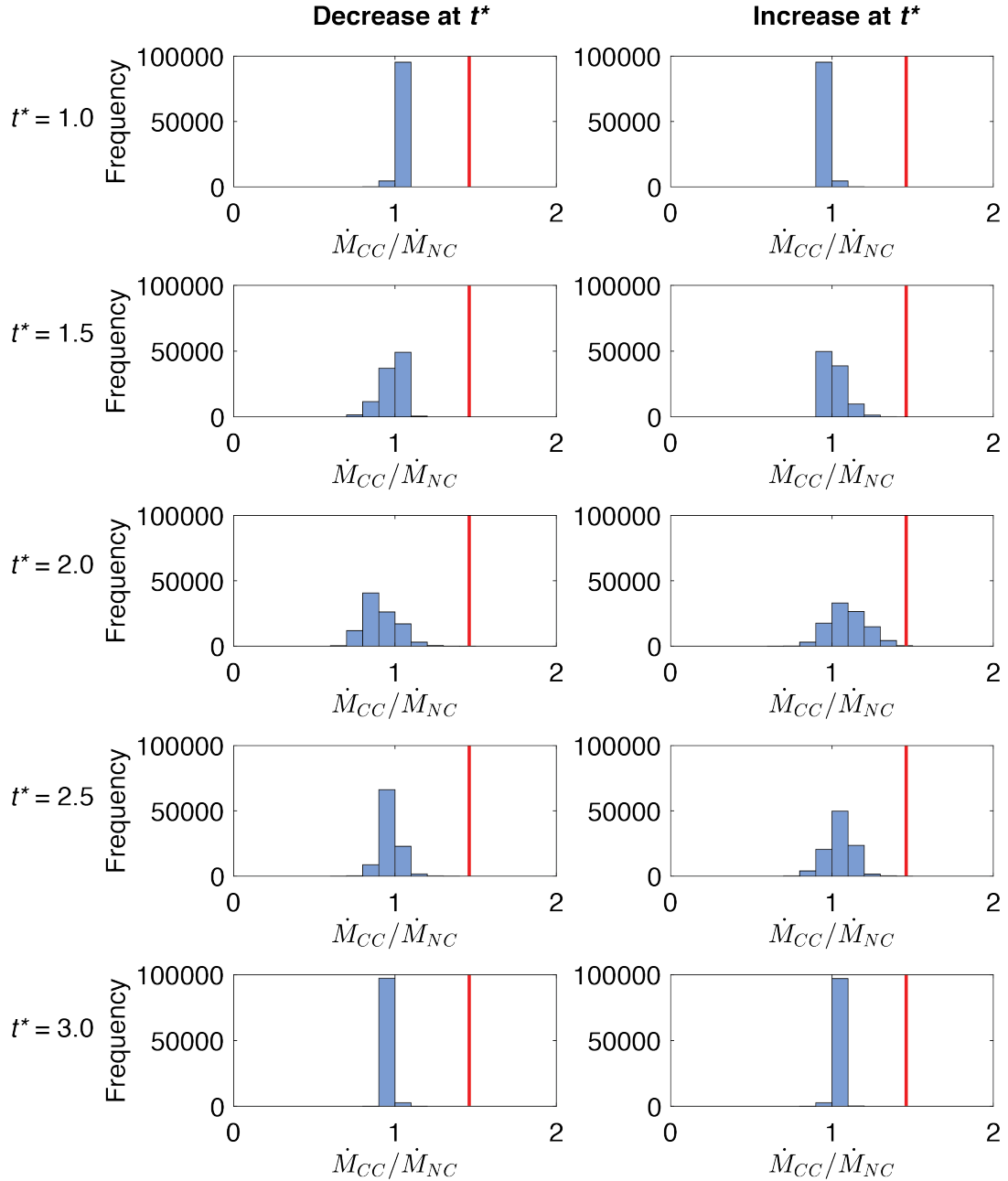
Fig. S9. Monte Carlo simulations assessing the possibility that a temporal change in accretion rates can explain the differences in accretion rates inferred from CO and LL paleointensities. Each plot shows a histogram of the mean accretion rate in the carbonaceous reservoir ($\dot{M}_{CC}$) over the mean accretion rate in the non-carbonaceous reservoir ($\dot{M}_{NC}$). Left column shows simulations for an accretion rate that decreases at t^*. Right column shows simulations for an accretion rate that increases at t^*. From top to bottom are simulations for different choices of t^*. Red line indicates the threshold ratio of 1.46.

disturbances of the Al-Mg system due to parent-body metamorphism (*63*). For the non-carbonaceous reservoir, we used a mean of $\mu = 2.0$ Ma after CAI-formation and a standard deviation of $\sigma = 0.1$ Ma, while for the carbonaceous reservoir we used a mean of $\mu = 2.4$ Ma after
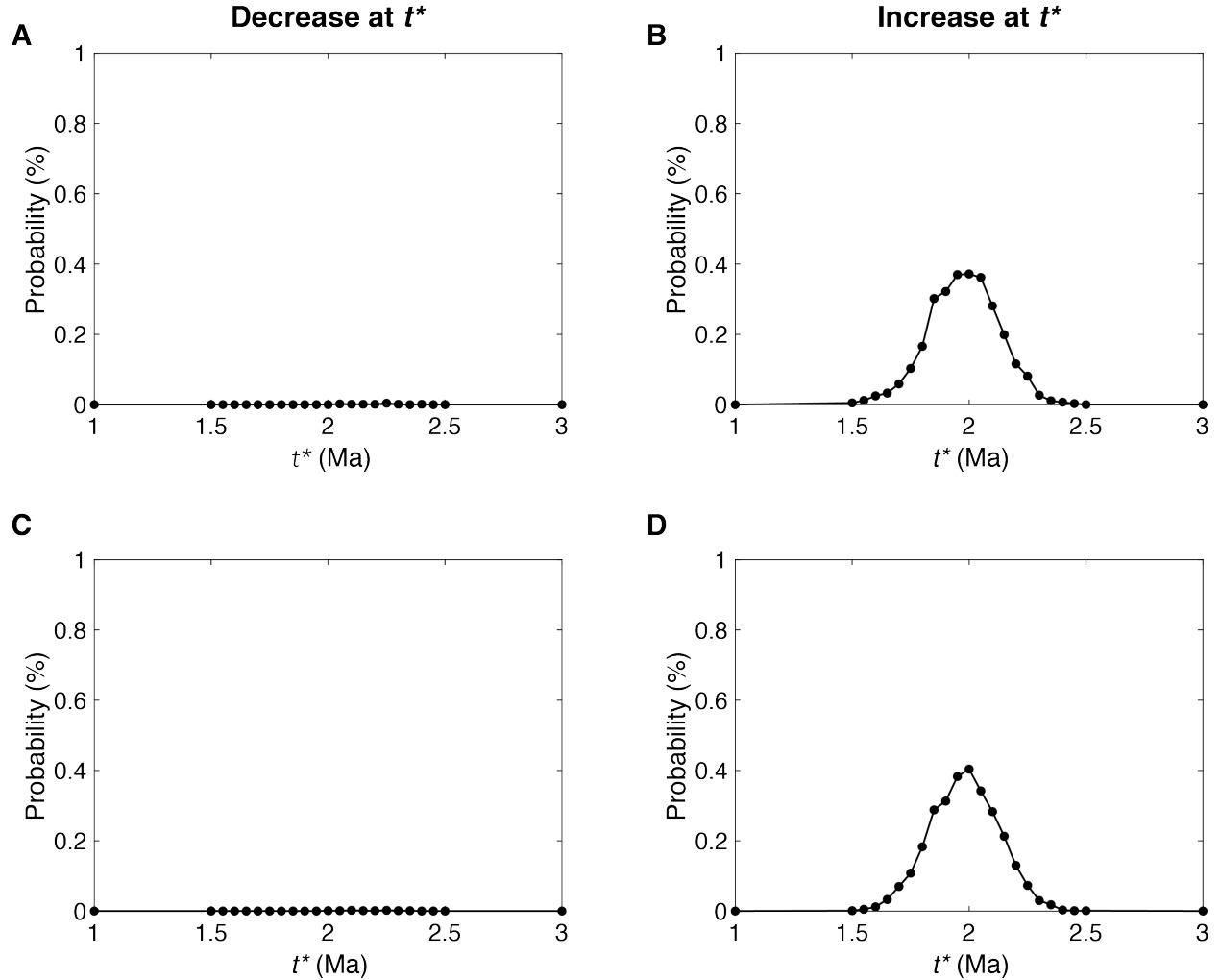
Fig. S10. Probabilities from Monte Carlo simulations. Each datapoint represents the percentage of cases from 100,000 simulations in which our measurements represent temporal variations. t^* represents the time that the accretion rate (left) decreases and (right) increases, assuming ages for the two reservoirs reported in ref. (11). **(A, B)** Assumes a threshold ratio of 33. **(C, D)** Assumes a threshold ratio of 1.46.

CAI-formation and a standard deviation of $\sigma = 0.2$ Ma. Experiments that had the ratio between the mean accretion rate in the carbonaceous reservoir to the mean accretion rate in the non-carbonaceous reservoir $\geq \dot{M}_{\text{high}}/\dot{M}_{low} \sim 33$ were taken as realizations that would satisfy that the measured magnetic fields [from ref. (11) and this study] support a time varying accretion rate in the first 3 Ma after CAI formation. The highest probability of such scenario was 32.7% (Table S6; Fig. S11A-B). We also assumed a ratio $\geq \dot{M}_{\text{high}}/\dot{M}_{low} \sim 1.46$ and the highest probability in this case was 32.4% (Table S6; Figs. S11C-D).

Overall, our simulations show that it is unlikely, even for the most conservative cases, that the samples obtained for this study and from previous measurements have recorded magnetic fields that are consistent with a temporal variation in solar accretion rate.
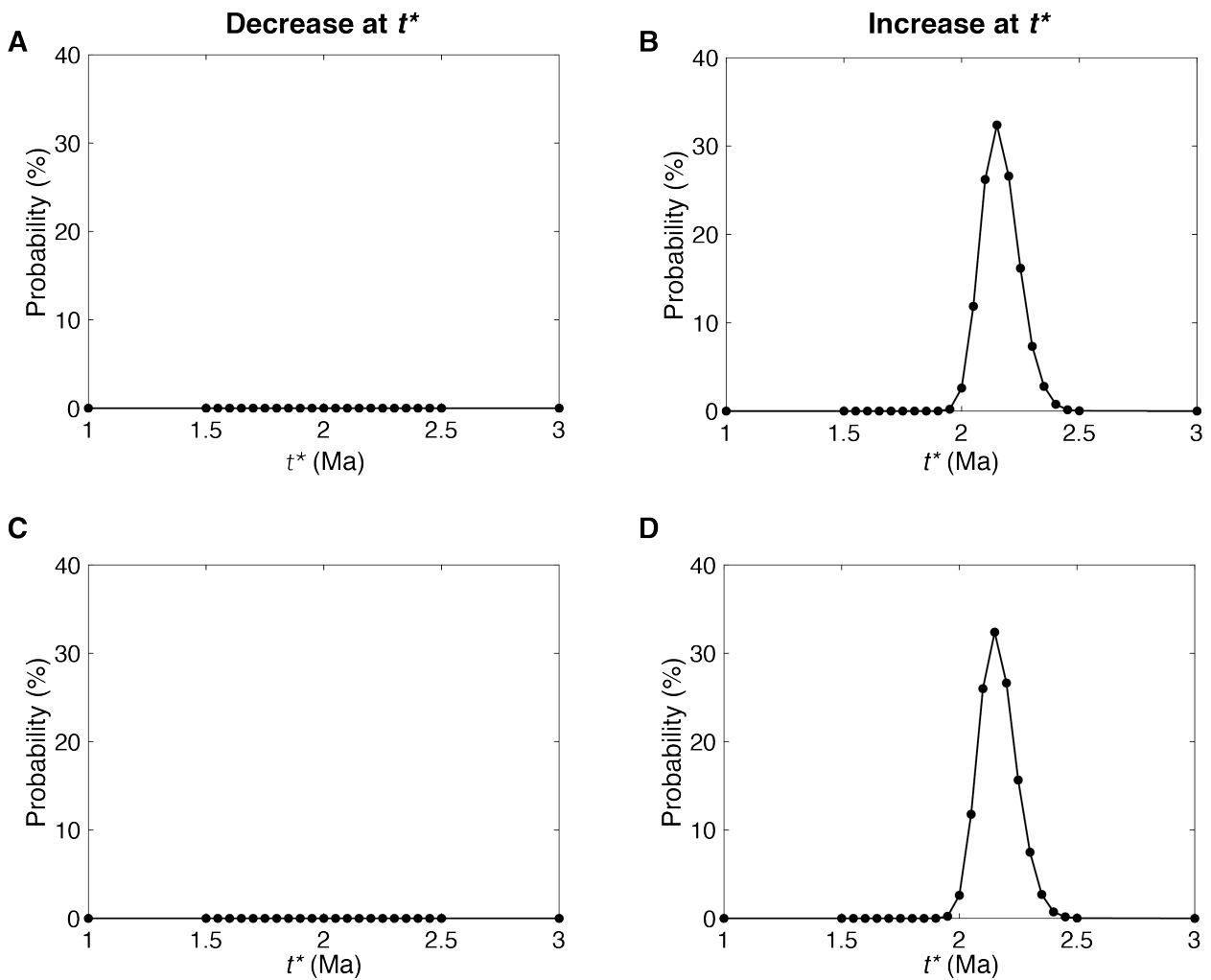
Fig. S11. Probabilities from Monte Carlo simulations. Each datapoint represents the percentage of cases from 100,000 simulations in which our measurements represent temporal variations. t^* represents the time that the accretion rate (left) decreases and (right) increases, assuming ages for the two reservoirs reported in refs. (*57-60*). **(A, B)** Assumes a threshold ratio of 33. **(C, D)** Assumes a threshold ratio of 1.46.

Sample	Meteorite	Orientation Measured	Distance to fusion crust (mm)	NRM (Am^2)	Averages (mT)	Component	Range (mT)	N	MAD not anc. (°)	DANG (°)	Anc.?	Dec. (°)	Inc. (°)	MAD (°)
DOC1	ALHA	N	3.3	5.6E-12	5-20; 40-90; 100-145	HC	0-160	8	28.1	9.1	Y	9.2	21.5	16
DOC2	ALHA	S	5.8	2.3E-11	50-145; 145-410	LC	0-10	3	11.9	-	N	197.4	-83.1	11.9
						HC	15-272	8	16.5	4.1	Y	76.5	-27.9	9.9
DOC3a	DOM	T	7	7.2E-12	10-30; 40-65; 80-100	LC	0-20	3	6.5	-	N	266.8	-75.1	6.5
						HC	20-90	11	23.1	8	Y	112.1	34.7	9.6
DOC3b	DOM	T	7	3.7E-12	25-35, 40-60	LC	0-5	2	0	-	N	195.7	65.6	0
						HC	5-50	6	32.1	14	Y	77.9	35.2	18.7
DOC4	DOM	B	7.5	4.9E-11	55-65; 70-100	LC	0-5	2	0	-	N	147.1	-39.3	0
						HC	5-85	12	16.8	37.7	N	305.1	10	16.8
DOC5a	DOM	B	8	4.3E-12	30-60	HC	0-45	4	23.3	53.9	N	297.5	48.6	23.3
DOC5b	DOM	B	8	1.7E-12	20-35; 35-75	HC	0-55	6	15.4	23.9	N	310.8	36.9	15.4
DOC6a	DOM	T	6	1.3E-12	40-50	HC	0-70	7	24.1	32.2	Y	59.9	-67.8	24.1
DOC6b	DOM	T	6	1.3E-10	55-100	HC	0-77.5	12	7.4	4	Y	15.7	-57.4	5.5

Table S1. Summary of PCAs of the dusty olivine chondrules. The first column lists the sample name, the second column lists the meteorite ("ALHA" for ALHA 77307 and "DOM" for DOM 08006), the third column lists the orientation of the sample as measured in magnetometer coordinates following the diagram from Fig. S1, the fourth column lists the magnetic moment of the NRM in Am^2, the fifth column lists the steps that were averaged in mT, the sixth column lists the name of the component ("LC" for low coercivity and "HC" for high coercivity), the seventh column lists the range used to calculate the fit in mT, the eighth column lists the number of steps used to calculate the component, the ninth column lists the maximum angle deviation (MAD) for the non-anchored component, the tenth column lists the deviation angle (DANG) for the component, the eleventh column denotes whether the component is anchored ("Y" for yes and "N" for no), the twelfth through fourteenth columns list the declination, inclination and MAD for the component.

Meteorite	N	Length of the resultant of the vectors (R)	Critical length of the resultant of the vectors (R_0)
ALHA 77307	2	1.51	1.85
DOM 08006	4	1.48	3.02

Table S2. Summary of the Watson's randomness test for each meteorite. The first column lists the meteorite name, the second column shows the number of chondrules, the third column shows the calculated length of the results of the vectors, the fourth column shows the critical length of the resultant of the vectors for a 95% confidence interval.

Sample	Analysis	SiO_2	TiO_2	Al_2O_3	Cr_2O_3	FeO	MnO	MgO	CaO	Na_2O	NiO	ZnO	Total
DOC2	Forsterite	42.52	0.00	0.02	0.40	0.87	0.30	56.64	0.14	-	-	-	100.89
	Forsterite	42.79	0.02	0.02	0.40	1.09	0.19	56.00	0.11	-	-	-	100.63
	Forsterite	42.55	0.01	0.02	0.38	0.72	0.22	56.18	0.24	-	-	-	100.33
	Forsterite	42.62	0.02	0.05	0.37	0.73	0.25	56.62	0.16	-	-	-	100.81
	Forsterite	42.58	0.01	0.03	0.32	0.69	0.24	56.54	0.14	-	-	-	100.55
	Magnetite	1.48	0.00	0.08	2.65	82.03	0.06	0.62	0.12	-	2.57	0.00	89.61
DOC6b	Forsterite	41.45	0.03	0.02	0.52	1.38	0.29	56.42	0.18	-	-	-	100.28
	Forsterite	41.67	0.00	0.03	0.49	1.84	0.28	57.30	0.18	-	-	-	101.79
	Forsterite	41.93	0.00	0.02	0.43	2.26	0.24	56.08	0.19	-	-	-	101.16
	Forsterite	41.88	0.00	0.02	0.50	1.40	0.19	56.50	0.20	-	-	-	100.70
	Forsterite	42.73	0.00	0.04	0.45	1.45	0.22	56.15	0.20	-	-	-	101.24
	Magnetite	0.93	0.00	0.02	0.21	88.11	0.04	1.30	0.01		2.34	0.00	92.97

Table S3. Summary of WDS analysis of forsterite and magnetite conducted in samples DOC2 and DOC6b. The first column shows the sample name, the second column shows the interpretation of the mineral, the third through thirteenth columns show the concentration of each element (weight percent), and the fourteenth column shows the sum of the percentages.

Sample	Analyses	Fe	Ni	Cr	Mn	P	S	O	Total
DOC2	Fe	93.64	0.06	0.91	0.05	0.03	0.03	3.55	98.26
	Fe	94.13	0.06	1.05	0.01	0.02	0.00	2.89	98.17
	Fe	93.36	0.06	1.21	0.11	0.03	0.02	4.18	98.97
	Fe,Ni	68.12	20.35	1.11	0.00	0.46	0.75	9.94	100.73
	Fe,Ni	77.82	4.59	0.66	0.04	0.45	0.45	11.43	95.44
DOC6b	Fe	97.57	0.03	0.29	0.00	0.02	0.00	0.36	98.27
	Fe	97.27	0.02	0.25	0.03	0.02	0.01	0.62	98.21
	Fe	97.16	0.04	0.30	0.05	0.03	0.02	1.36	98.95

Table S4. Summary of WDS analysis of metal grains in samples DOC2 and DOC6b. The first column shows the sample name, the second column shows the interpretation of the mineral, the third through seventh columns show the concentration of each element (weight percent), and the eighth column shows the sum of the percentages.

Sample	Meteorite	Range (mT)	N	ρ	Fit Type	Paleointensity (μT)	95% Confidence Interval (μT)
DOC1	ALHA	0-100	61	0.7	RMA	25.3	4.8
DOC2	ALHA	20-115	60	0.8	RMA	35.3	6.4
					ALHA mean	**30**	
					95% confidence Interval	**10**	
DOC3a	DOM	20-75	72	0.2	OLS	20.5	26.3
DOC3b	DOM	5-50	60	0.9	RMA	55.9	6.9
DOC4	DOM	5-90	108	0.8	RMA	30	3.9
DOC5b	DOM	5-55	50	0.7	RMA	102.1	19.2
DOC6b	DOM	5-50	60	1	RMA	85.1	6.7
					DOM mean	**59**	
					95% confidence Interval	**31**	
					Mean Paleointensity	**51**	
					95% confidence Interval	**24**	
					Corrected Mean Paleointensity	**101**	
					95% confidence Interval	**48**	

Table S5. Summary of the statistics of the paleointensity of the dusty olivine chondrules. The first column lists the sample name, the second column lists the meteorite ("ALHA" for ALHA 77307 and "DOM" for DOM 08006), the third column lists the AF range used for the fit to in mT, the fourth lists the number of measurements used in the fit to ΔNRM versus ΔARM, the fifth column lists the correlation coefficient associated with fits, the sixth column lists the fit type ("RMA" for reduced major axis and "OLS" for ordinary least squares), the seventh column lists the paleointensity calculated from the fit in μT, and the eighth column lists the 95% confidence interval of the fit. For each meteorite, we also show the mean and the 95% confidence interval. At the bottom, we list the grand mean and the grand mean corrected for chondrule spin along with their 95% confidence intervals.

	Probability of Temporal Variation in Accretion Rate				

Threshold ≥ 33
R_{NC} = 2 AU, R_{CC} = 5 AU **Time of field change (t^*, Ma after CAI formation)**
Ages from ref. (11)

	1.0	1.5	2.0	2.5	3.0
Field decreases at t^*	0%	0%	0%	0%	0%
Field increases at t^*	0%	0.005%	0.372%	0%	0%

Threshold ≥ 1.46
R_{NC} = R_{CC} = 3 AU **Time of field change (t^*, Ma after CAI formation)**
Ages from ref. (11)

	1.0	1.5	2.0	2.5	3.0
Field decreases at t^*	0%	0%	0.001%	0%	0%
Field increases at t^*	0%	0.001%	0.404%	0.001%	0%

Threshold ≥ 33
R_{NC} = R_{CC} = 3 AU **Time of field change (t^*, Ma after CAI formation)**
Ages from refs. (*57-60*)

	1.0	1.5	2.15	2.5	3.0
Field decreases at t^*	0%	0%	0%	0%	0%
Field increases at t^*	0%	0%	32.372%	0.026%	0%

Threshold ≥ 1.46
R_{NC} = R_{CC} = 3 AU **Time of field change (t^*, Ma after CAI formation)**
Ages from refs. (*57-60*)

	1.0	1.5	2.15	2.5	3.0
Field decreases at t^*	0%	0%	0%	0%	0%
Field increases at t^*	0%	0%	32.388%	0.003%	0%

Table S6. Summary of selected Monte Carlo simulations used to the determine the probability that the measurements considered in this study represent a time variation in the accretion rate. Shown are the probabilities for two distinct thresholds values, two distinct locations for the carbonaceous and non-carbonaceous reservoirs, and two distinct set of ages. The two distinct thresholds (see Section 5) represent the ratio between the accretion rate in the carbonaceous reservoir and the accretion rate in the non-carbonaceous reservoir. Columns two through six show the probabilities for the nebular field changing at a time t^*, where $t^* = 1, 1.5, 2, 2.5$ and 3.0 Ma after CAI formation, respectively. The first row of each table shows the probability for the cases in which the accretion rate increases at t^*, while the second row of each table shows the probability for the cases in which the accretion rate decreases at t^*.

REFERENCES AND NOTES

1. S. M. Andrews, Observations of protoplanetary disk structures. *Annu. Rev. Astron. Astrophys.* **58**, 483–528 (2020).

2. T. S. Kruijer, T. Kleine, L. E. Borg, The great isotopic dichotomy of the early solar system. *Nat. Astron.* **4**, 32–40 (2020).

3. E. R. D. Scott, A. N. Krot, I. S. Sanders, Isotopic dichotomy among meteorites and its bearing on the protoplanetary disk. *Astrophys. J.* **854**, 164 (2018).

4. T. Kleine, G. Budde, C. Burkhardt, T. S. Kruijer, E. A. Worsham, A. Morbidelli, F. Nimmo, The non-carbonaceous–carbonaceous meteorite dichotomy. *Space Sci. Rev.* **216**, 55 (2020).

5. R. Brasser, S. J. Mojzsis, The partitioning of the inner and outer solar system by a structured protoplanetary disk. *Nat. Astron.* **4**, 492–499 (2020).

6. T. Lichtenberg, J. Drążkowska, M. Schönbächler, G. J. Golabek, T. O. Hands, Bifurcation of planetary building blocks during Solar System formation. *Science*. **371**, 365–370 (2021).

7. X.-N. Bai, J. Goodman, Heat and dust in active layers of protostellar disks. *Astrophys. J.* **701**, 737–755 (2009).

8. X.-N. Bai, Global simulations of the inner regions of protoplanetary disks with comprehensive disk microphysics. *Astrophys. J.* **845**, 75 (2017).

9. N. J. Turner, S. Fromang, C. Gammie, H. Klahr, G. Lesur, M. Wardle, X.-N. Bai, in *Protostars and Planets VI*, H. Beuther, R. S. Klessen, C. P. Dullemond, T. K. Henning, Eds. (University of Arizona Press, 2014), pp. 411–432.

10. B. P. Weiss, X.-N. Bai, R. R. Fu, History of the solar nebula from meteorite paleomagnetism. *Sci. Adv.* **7**, eaba5967 (2021).

11. R. R. Fu, B. P. Weiss, E. A. Lima, R. J. Harrison, X.N. Bai, S. J. Desch, D. S. Ebel, C. Suavet, H. Wang, D. Glenn, D. le Sage, T. Kasama, R. L. Walsworth, A. T. Kuan, Solar nebula magnetic fields recorded in the Semarkona meteorite. *Science* **346**, 1089–1092 (2014).

12. N. T. Kita, T. Ushikubo, Evolution of protoplanetary disk inferred from ^{26}Al chronology of individual chondrules. *Meteorit. Planet. Sci.* **47**, 1108–1119 (2011).

13. C. Cournède, J. Gattacceca, M. Gounelle, P. Rochette, B. P. Weiss, B. Zanda, An early solar system magnetic field recorded in CM chondrites. *Earth Planet. Sci. Lett.* **410**, 62–74 (2015).

14. R. R. Fu, P. Kehayias, B. P. Weiss, D. L. Schrader, X.-N. Bai, J. B. Simon, Weak magnetic fields in the outer solar nebula recorded in CR chondrites. *J. Geophys. Res.*, **125**, e2019JE006260 (2020).

15. R. R. Fu, M. W. R. Volk, D. Bilardello, D. Libourel, G. R. J. Lesur, O. Ben Dor, The fine-scale magnetic history of the Allende meteorite: implications for the structure of the solar nebula. *AGU Adv.* **2**, e2021AV000486 (2021).

16. D. L. Schrader, K. Nagashima, A. N. Krot, R. C. Ogliore, Q.Z. Yin, Y. Amelin, C. H. Stirling, A. Kaltenbach, Distribution of ^{26}Al in the CR chondrite chondrule-forming region of the protoplanetary disk. *Geochim. Cosmochim. Acta* **201**, 275–302 (2017).

17. L. Carporzen, B. P. Weiss, L. T. Elkins-Tanton, D. L. Shuster, D. S. Ebel, J. Gattacceca, Magnetic evidence for a partially differentiated carbonaceous chondrite parent body. *Proc. Natl. Acad. Sci. U.S.A.* **108**, 6386–6389 (2011).

18. H. Wang, B. P. Weiss, X.-N. Bai, B. G. Downey, J. Wang, J. Wang, C. Suavet, R. R. Fu, M. E. Zucolotto, Lifetime of the solar nebula constrained by meteorite paleomagnetism. *Science* **355**, 623–627 (2017).

19. L. Bonal, M. Bourot-Denise, E. Quirico, G. Montagnac, E. Lewin, Organic matter and metamorphic history of CO chondrites. *Geochim. Cosmochim. Acta* **71**, 1605–1623 (2007).

20. J. Davidson, C. M. O'D. Alexander, R. M. Stroud, H. Busemann, L. R. Nittler, Mineralogy and petrology of Dominion Range 08006: A very primitive CO3 carbonaceous chondrite. *Geochim. Cosmochim. Acta* **265**, 259–278 (2019).

21. C. M. O'D. Alexander, R. C. Greenwood, R. Bowden, J. M. Gibson, K. T. Howard, I. A. Franchi, A mutli-technique search for the most primitive CO chondrites. *Geochim. Cosmochim. Acta* **221**, 406–420 (2018).

22. E. R. D. Scott, K. Keil, D. Stöffler, Shock metamorphism of carbonaceous chondrites. *Geochim. Cosmochim. Acta* **56**, 4281–4293 (1992).

23. C. M. O'D. Alexander, M. Fogel, H. Yabuta, G. D. Cody, The origin and evolution of chondrites recorded in the elemental and isotopic compositions of their macromolecular organic matter. *Geochim. Cosmochim. Acta* **71**, 4380–4403 (2007).

24. J. Shah, W. Williams, T. P. Almeida, L. Nagy, A. R. Muxworthy, A. Kovács, M. A. Valdez-Grijalva, K. Fabian, S. S. Russell, M. J. Genge, The oldest magnetic record in our solar system identified using nanometric imaging and numerical modeling. *Nat. Commun.* **9**, 1–6 (2018).

25. J. F. Einsle, R. J. Harrison, T. Kasama, P. Ó. Conbhuí, K. Fabian, W. Williams, L. Woodland, R. R. Fu, B. P. Weiss, P. A. Midgley, Multi-scale three-dimensional characterization of iron particles in

dusty olivine: Implications for paleomagnetism of chondritic meteorites. *Am. Mineral.* **101**, 2070–2084 (2016).

26. S.-C. L. L. Lappe, N. S. Church, T. Kasama, A. B. da Silva Fanta, G. Bromiley, R. E. Dunin-Borkowski, J. M. Feinberg, S. Russell, R. J. Harrison, Mineral magnetism of dusty olivine: A credible recorder of pre-accretionary remanence. *Geochem. Geophys. Geosyst.* **12**, Q12Z35 (2011).

27. S.-C. L. L. Lappe, J. M. Feinberg, A. Muxworthy, R. J. Harrison, Comparison and calibration of nonheating paleointensity methods : A case study using dusty olivine. *Geochem. Geophys. Geosyst.* **14**, 2143–2158 (2013).

28. E. R. D. Scott, A. N. Krot, in *Treatise on Geochemistry*, vol. 2 of *Planets, Asteroids, Comets, and the Solar System*, H. D. Holland, K. K. Turekian, Eds. (Elsevier Science, 2013), pp. 66–137.

29. S. J. Desch, M. A. Morris, H. C. Connolly Jr., A. P. Boss, The importance of experiments: Constraints on chondrule formation models. *Meteorit. Planet. Sci.* **47**, 1139–1156 (2012).

30. S. J. Desch, M. A. Morris, H. C. Connolly Jr., A. P. Boss, A critical examination of the X-wind model for chondrule and calcium-rich, aluminum-rich inclusion formation and radionuclide production. *Astrophys. J.* **725**, 692–711 (2010).

31. Recent high-precision Al-Mg ages of LL chondrules support a shorter formation interval than previous Al-Mg ages. See Supplementary Text for more information.

32. B. P. Weiss, E. A. Lima, L. E. Fong, F. J. Baudenbacher, Paleomagnetic analysis using SQUID microscopy. *J. Geophys. Res.* **112**, B09105 (2007).

33. L. Nagy, W. Williams, L. Tauxe, A. R. Muxworthy, I. Ferreira, Thermomagnetic recording fidelity of nanometer-sized iron and implications for planetary magnetism. *Proc. Natl. Acad. Sci. U.S.A.* **116**, 1984–1991 (2019).

34. G. S. Watson, A test for randomness of directions. *Geophys. J. Int.* **7**, 160–161 (1956).

35. S. M. Tikoo, B. P. Weiss, W. S. Cassata, D. L. Shuster, J. Gattacceca, E. A. Lima, C. Suavet, F. Nimmo, M. D. Fuller, Decline of the lunar core dynamo. *Earth Planet. Sci. Lett.* **404**, 89–97 (2014).

36. L. Hartmann, N. Calvet, E. Gullbring, P. D'Alessio, Accretion and the evolution of T Tauri disks. *Astrophys. J.* **495**, 385–400 (1998).

37. L. Hartmann, G. Herczeg, N. Calvet, Accretion onto pre-main-sequence stars. *Annu. Rev. Astron. Astrophys.* **54**, 135–180 (2016).

38. S. K. Atreya, A. Crida, T. Guillot, J. I. Lunine, N. Madhusudhan, O. Mousis, in *Saturn in the 21st Century*, K. H. Baines, F. M. Flasar, N. Krupp, T. Stallard, Eds. (Cambridge Univ. Press, 2018), pp. 5–43.

39. C. J. Clarke, A. Gendrin, M. Sotomayor, The dispersal of circumstellar discs: The role of the ultraviolet switch. *Mon. Not. R. Astron. Soc.* **328**, 485–491 (2001).

40. J. E. Owen, C. J. Clarke, B. Ercolano, On the theory of disc photoevaporation. *Mon. Not. R. Astron. Soc.* **422**, 1880–1901 (2012).

41. G. Picogna, B. Ercolano, J. E. Owen, M. L. Weber, The dispersal of protoplanetary discs – I. A new generation of X-ray photoevaporation models. *Mon. Not. R. Astron. Soc.* **487**, 691–701 (2019).

42. L. Wang, X.-N. Bai, J. Goodman, Global simulations of protoplanetary disk outflows with coupled non-ideal magnetohydrodynamics and consistent thermochemistry. *Astrophys. J.* **874**, 90 (2019).

43. X.-N. Bai, Toward a global evolutionary model of protoplanetary disks. *Astrophys. J.* **821**, 80 (2016).

44. T. K. Suzuki, M. Ogihara, A. Morbidelli, A. Crida, T. Guillot, Evolution of protoplanetary discs with magnetically driven disc winds. *Astron. Astrophys.* **596**, A74 (2016).

45. G. P. Rosotti, B. Ercolano, J. E. Owen, P. J. Armitage, The interplay between x-ray photoevaporation and planet formation. *Mon. Not. R. Astron. Soc.* **430**, 1392–1401 (2013).

46. J. L. Kirschvink, R. E. Kopp, T. D. Raub, C. T. Baumgartner, J. W. Holt, Rapid, precise, and high-sensitivity acquisition of paleomagnetic and rock-magnetic data: Development of a low-noise automatic sample changing system for superconducting rock magnetometers. *Geochem. Geophys. Geosyst.* **9**, Q05Y01 (2008),.

47. A. Stephenson, Three-axis static field demagnetization of rocks and the identification of natural remanent magnetization, gyroremanent magnetization, and anisotropy. *J. Geoph. Res.* **98**, 373–381 (1993).

48. E. A. Lima, B. P. Weiss, Ultra-high sensitivity moment magnetometry of geological samples using magnetic microscopy. *Geochem. Geophys. Geosyst.* **17**, 3754–3774 (2016).

49. J. L. Kirschvink, The least-squares line and plane and the analysis of palaeomagnetic data. *Geophys. J. R. Astr. Soc.* **62**, 699–718 (1980).

50. L. Tauxe, H. Staudigel, Strength of the geomagnetic field in the Cretaceous Normal Superchron: New data from submarine basaltic glass of the Troodos Ophiolite. *Geochem. Geophys. Geosyst.* **5**, Q02H06 (2004).

51. R. J. Smith, Use and misuse of the reduced major axis for line-fitting. *Am. J. Phys. Anthropol.* **140**, 476–486 (2009).

52. J. T. Armstrong, CITZAF: A package of correction programs for the quantitative electron microbeam X-ray analysis of thick polished materials, thin films, and particles. *Microbeam Anal.* **4**, 177–200 (1995).

53. R. R. Fu, E. A. Lima, M. W. R. Volk, R. Trubko, High sensitivity moment magnetometry with the quantum diamond microscope. *Geochem. Geophys. Geosyst.*, **21**, e2020GC009147 (2020).

54. D. R. Glenn, R. R. Fu, P. Kehayias, D. Le Sage, E. A. Lima, B. P. Weiss, R. L. Walsworth, Micrometer-scale magnetic imaging of geological samples using a quantum diamond microscope. *Geochem. Geophys. Geosyst.* **18**, 3254–3267 (2017).

55. S. Ebert, J. Render, G. A. Brennecka, C. Burkhardt, A. Bischoff, S. Gerber, T. Kleine, Ti isotopic evidence for a non-CAI refractory component in the inner solar system. *Earth Planet. Sci. Lett.* **498**, 257–265 (2018).

56. J. M. Schneider, C. Burkhardt, Y. Marrocchi, G. A. Brennecka, T. Kleine, Early evolution of the solar accretion disk inferred from Cr-Ti-O isotopes in individual chondrules. *Earth Planet. Sci. Lett.* **551**, 116585 (2020).

57. F. E. DeMeo, B. Carry, Solar system evolution from compositional mapping of the asteroid belt. *Nature* **505**, 629–634 (2014).

58. A. Morbidelli, K. J. Walsh, D. P. O'Brien, D. A. Minton, W. F. Bottke, in *Asteroids IV*, P. Michel, F. E. DeMeo, W. F. Bottke, Eds. (University of Arizona, 2015), pp. 493–507.

59. S. Sutton, C.M.O.'D. Alexander, A. Bryant, A. Lanzirotti, M. Newville, E. A. Cloutis, The bulk valence state of Fe and the origin of water in chondrites. *Geochim. Cosmochim. Acta* **211**, 115–132 (2017).

60. L. Testi, T. Birnstiel, L. Ricci, S. Andrews, J. Blum, J. Carpenter, C. Dominik, A. Isella, A. Natta, J. P. Williams, D. J. Wilner, in *Protostars and Planets VI*, H. Beuther, R. S. Klessen, C. P. Dullemond, T. K. Henning, Eds. (University of Arizona Press, 2014), pp. 339–361.

61. S. J. Desch, A. Kalyaan, C. M. O.'D. Alexander, The effect of Jupiter's formation on the distribution of refractory elements and inclusions in meteorites. *Astrophys. J. Suppl. S.* **238**, 11 (2018).

62. P. A. Selkin, J. S. Gee, L. Tauxe, W. P. Meurer, A. J. Newell, The effect of remanence anisotropy on paleointensity estimates: A case study from the Archean Stillwater Complex. *Earth Planet. Sci. Lett.* **183**, 403–416 (2000).

63. G. Siron, K. Fukuda, M. Kimura, N. T. Kita, New constraints from ^{26}Al-^{26}Mg chronology of anorthite bearing chondrules in unequilibrated ordinary chondrites. *Geochim. Cosmochim. Acta* **293**, 103–126 (2021).

64. G. Siron, N. T. Kita, K. Fukuda, M. Kimura, in *Lunar and Planetary Science Conference* (2021), p. 1639.

65. A. T. Hertwig, M. Kimura, T. Ushikubo, C. Defouilloy, N. T. Kita, The ^{26}Al-^{26}Mg systematics of FeO-rich chondrules from Acfer 094: Two chondrule generations distinct in age and oxygen isotope ratios. *Geochim. Cosmochim. Acta* **253**, 111–126 (2019).

66. K. Nagashima, A. N. Krot, M. Komatsu, ^{26}Al–^{26}Mg systematics in chondrules from Kaba and Yamato 980145 CV3 carbonaceous chondrites. *Geochim. Cosmochim. Acta* **201**, 303–319 (2017).